Numerical study of turbulent two-phase Couette flow

By A.Y. Ovsyannikov, D. Kim†, A. Mani AND P. Moin

1. Motivation and objectives

The motivation underpinning this work is the need to understand bubble generation mechanisms due to interactions between free surface and turbulent boundary layers as commonly seen near ship walls. As a canonical problem, we consider a turbulent plane Couette flow with vertical parallel sidewalls and an air-water interface established by gravity in the vertical direction. Two-phase Couette flow has been described in the literature in different flow setups. Most studies were limited to cases of low Reynolds number and the evolution of a single bubble/droplet. Deformation and breakup of a single droplet in a plane Couette flow at low Reynolds number has been studied experimentally, theoretically, and numerically (see e.g., Li *et al.* 2000; Renardy *et al.* 2002; Rallison 1984). In another example of the two-phase Couette flow is the two-layers of immiscible fluids which are set between moving horizontal walls. Due to viscosity difference between fluids, there is a jump in the tangential velocity gradient across the interface which induces instabilities at the fluid interface (Coward *et al.* 1997; Charru & Hinch 2000).

At high Reynolds number, there are only a few studies of two-phase Couette flow. Iwasaki *et al.* (2001) studied the dynamics of a single immiscible drop in turbulent gas flow between two moving walls. Fulgosi *et al.* (2003); Liu *et al.* (2009) performed direct numerical simulation (DNS) of interface evolution in Couette flow between two moving horizontal walls. One interesting case of a two-phase Couette flow in a turbulent regime is when the initial interface is set to be orthogonal to the moving vertical walls. In such a setup, the interaction between the fluid interface and the turbulent boundary layer is a key phenomenon. At sufficiently high Reynolds, Weber and Froude numbers, shear-induced interfacial waves can break, which leads to the formation of air cavities. These air cavities will be further fragmented by turbulence to smaller bubbles. These complexities make two-phase Couette flow at high Reynolds number a challenging problem for both experiments and numerical analysis. Capturing the small-scale flow and interface features requires high-resolution experimental techniques and very expensive DNS calculations. Only two numerical studies (Kim *et al.* 2012, 2013) have been performed for investigation of air entrainment and bubble generation in two-phase Couette flow.

The current work is a continuation of our recent studies (Kim *et al.* 2012, 2013), where we performed numerical simulations of the interface breakup in two-phase Couette flow at Reynolds number of approximately 13000 and Weber number of approximately 42000 (surface tension coefficient was much smaller than the realistic value for an air-water system). The effect of Froude number on the interface breakup and bubble generation was studied in Kim *et al.* (2012). The second paper of Kim *et al.* (2013) was mostly devoted to the development and assessment of a mass conservative interface-capturing method based on a geometric volume-of-fluid (VOF) approach, and one simulation of

† Cascade Technologies Inc.

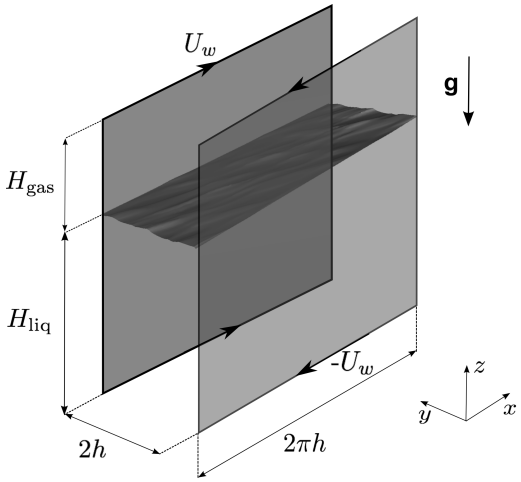

FIGURE 1. Schematic illustration of the flow geometry.

the two-phase Couette flow was performed for a Reynolds number of 12000 and a Weber number of 200. However, there have been no studies with one-to-one matched experiments and numerical simulations. The primary objective of this work is to perform a numerical simulation of a two-phase Couette flow with flow parameters very close to those of the laboratory experiment conducted by our collaborators (the group of Dr. James Duncan at the University of Maryland). The bubble formation rate, bubble size distribution, and the effect of interface on the modulation of turbulence are the main characteristics of this flow type, and our investigations are focused on understanding these characteristics.

This paper is structured as follows. In Section 2 we present the equations for the problem and discuss the key dimensions chosen for our simulations, grid resolution requirements and details of the numerical method. Preliminary results of the numerical simulation are presented and analyzed in Section 3. In Section 4 we show the effect of water depth on air entrainment. Finally, conclusions are summarized in Section 5.

2. Problem formulation

We perform a simulation of a two-phase system with realistic air/water density and viscosity ratios. The density of liquid is $\rho_{\text{liq}} = 1000\,\text{kg/m}^3$ and the density of gas is $\rho_{\text{gas}} = 1.2\,\text{kg/m}^3$. However, to reduce computational cost, the viscosity of gas and liquid are increased four times compared to their realistic values. Thus the viscosity of the gaseous phase is $\mu_{\text{gas}} = 7.2 \times 10^{-5}\,\text{Pa}\cdot\text{s}$ and the viscosity of the liquid phase is $\mu_{\text{liq}} = 4 \times 10^{-3}\,\text{Pa}\cdot\text{s}$. The surface tension coefficient σ and gravity acceleration $\mathbf{g}$ take realistic values of $0.07\,\text{N/m}$ and $9.81\,\text{m/s}^2$, respectively. Figure 1 depicts the schematic of the flow configuration and domain size. The computational domain is a rectangular box with sizes $2\pi h$, $2h$ and $6h$ in the streamwise (x), wall-normal (y) and spanwise (z) directions, respectively. Here $h = 2\,\text{cm}$ is the half-distance between walls. Initially, the interface is located at a plane $z = 4h$, hence a height of liquid layer H_{liq} is $4h$ and a height of gas layer H_{gas} is $2h$. The sidewalls are moving in the opposite directions with speed of $U_{\text{w}} = 1.6\,\text{m/s}$. Based on the chosen parameters, the following main dimensionless

	Re	We	Fr	$\rho_{\rm liq}/\rho_{\rm gas}$	$\mu_{\rm liq}/\mu_{\rm gas}$	$H_{\rm liq}/h$
Simulation (Kim *et al.* 2012)	12760	41600	3.9, 6.8	833.33	50	1.57
Simulation (Kim *et al.* 2013)	12000	206	3.8	833.33	55.55	1.57
Exp. (Masnadi *et al.* 2013)	46750-74750	837-2142	2.06-3.29	833.33	55.55	18.7
Exp. (Washuta *et al.* 2014)	32000	730	3.6	833.33	55.55	35
Present simulation	8000	730	3.6	833.33	55.55	4

TABLE 1. Flow configurations for two-phase turbulent Couette flow from experimental and numerical studies. In Masnadi *et al.* (2013), dimensionless parameters were defined in a different way. Here we recompute all parameters according to Eq. (2.1).

parameters are

$$\mathrm{Re} = \frac{\rho_{\rm liq} U_{\rm w} h}{\mu_{\rm liq}}, \quad \mathrm{We} = \frac{\rho_{\rm liq} U_{\rm w}^2 h}{\sigma}, \quad \mathrm{Fr} = \frac{U_{\rm w}}{\sqrt{gh}}, \quad \mathrm{ar} = \frac{H_{\rm liq}}{h}, \tag{2.1}$$

which are Reynolds, Weber, Froude numbers, and aspect ratio (ratio of water depth to h), respectively. All non-dimensional groups are determined using properties of the liquid phase. In the current study, Re = 8000, We = 730, Fr = 3.6 and ar = 4.

Table 1 summarizes recent experiments and numerical studies on the two-phase Couette flow problem in turbulent regime. The experiments reported in Table 1 are all performed by Masnadi *et al.* (2013) in a $7.5\,\mathrm{m} \times 0.075\,\mathrm{m} \times 1\,\mathrm{m}$ air-water channel at different operating parameters. In their setup one wall is stationary and the other is moving. The belt velocity is varied in a range from 2.5 to 4.0 m/s, leading to a range of Reynolds numbers from 46750 to 74750, Weber numbers from 837 to 2142, and Froude numbers from 2.06 to 3.29. Note that there have been no studies with one-to-one matched experiments and numerical simulations, in particular concerning the matching of such key dimensionless parameters as Re, We and Fr. In the present work we selected these parameters in accordance with the experiments being performed currently by our collaborators for a channel of width $h = 2\,\mathrm{cm}$ (Washuta *et al.* 2014) and Reynolds number of 32000, Weber number of 730 and Froude number of 3.6. These match with the experiment in the narrow channel Weber and Froude numbers, density and viscosity ratios; however, the Reynolds number is four times lower in our numerical study. We expect that a four fold difference in Reynolds number should not be critical in predicting bubble generation due to the large difference between turbulent and interfacial length scales (see paragraph 2.3 for an estimation of Kolmogorov and Hinze scales). Also, the aspect ratio in simulations is much smaller than in experiments.

2.1. *Governing equations and numerical method*

The governing equations describing the motion of two immiscible, incompressible Newtonian fluids are the conservation of mass and momentum. The first equation is given in terms of the volume fraction function ψ as

$$\frac{\partial \psi}{\partial t} + \nabla \cdot (\psi \mathbf{u}) = 0, \tag{2.2}$$

and the second is

$$\frac{\partial \rho \mathbf{u}}{\partial t} + \nabla \cdot (\rho \mathbf{u}\mathbf{u}) = -\nabla p + \nabla \cdot \tau + \rho \mathbf{g} + \mathbf{F}_{\mathrm{st}}, \tag{2.3}$$

where $\mathbf{u}$ is the velocity, p is the pressure, ρ is the density, $\tau = \mu(\nabla \mathbf{u} + \nabla \mathbf{u}^T)$ is the shear stress tensor, μ is the dynamic viscosity, $\mathbf{g}$ is the acceleration due to gravity and $\mathbf{F}_{\mathrm{st}} = \sigma \kappa \delta_\Sigma \mathbf{n}$ is the surface tension force. Here, σ is the surface tension coefficient, δ_Σ is the Dirac delta function, κ is the interface curvature, and $\mathbf{n}$ is the interface normal vector. The volume fraction function ψ is equal to 1 in the gas phase and 0 in the liquid phase. The interface is then represented by the volume fraction values, $0 < \psi < 1$. In the case of a two-phase flow with immiscible fluids, the density and dynamic viscosity are the stepwise functions and can be written in terms of ψ,

$$\rho(\mathbf{x}, t) = \rho_{\mathrm{gas}} \psi(\mathbf{x}, t) + \rho_{\mathrm{liq}} \left[1 - \psi(\mathbf{x}, t)\right], \tag{2.4}$$

$$\mu(\mathbf{x}, t) = \mu_{\mathrm{gas}} \psi(\mathbf{x}, t) + \mu_{\mathrm{liq}} \left[1 - \psi(\mathbf{x}, t)\right]. \tag{2.5}$$

For discretization of Eqs. (2.2)-(2.3), we use numerical schemes as described in Kim *et al.* (2013). In brief, we use the finite-volume pressure-correction method, where the interface dynamics is captured by the volume-of-fluid method. Geometric flux reconstruction is based on a piecewise line interface calculation (PLIC) algorithm. The VOF method conserves the mass of each phase within machine precision, and this is essential for simulation of two-phase flows at high Reynolds and Weber numbers. The surface tension force is computed using the continuum surface force model (Brackbill *et al.* 1992) coupled with the balanced force method (Francois *et al.* 2006). For an accurate calculation of interface normal vector and curvature, a level set function is used which is reconstructed from the ψ field at every timestep using a fast marching method (Sethian 1999).

2.2. *Initial and boundary conditions*

The flow is assumed to be statistically homogeneous in the streamwise x direction where periodic boundary conditions are used. On the side counter-moving walls ($y = \pm h$), we use no-slip boundary conditions. On the top and bottom walls ($z = 0$ and $z = 6h$), we use slip boundary conditions. On all solid wall boundaries, no-flux conditions are used for the volume fraction function. As the initial condition, we use a laminar velocity profile perturbed by 10% noise. The initial value for ψ corresponds to the flat shape of the interface.

2.3. *Grid resolution requirement*

In order to accurately capture the interface dynamics, we need to resolve the typical interface scale (r_{cr}) and turbulent scales (η and δ_ν).

2.3.1. *Turbulent lengthscale*

The Kolmogorov lengthscale is given by

$$\eta = (\nu^3/\varepsilon)^{1/4} \approx 110\,\mu\mathrm{m}. \tag{2.6}$$

Here ε is the mean energy dissipation rate per unit mass and it can be estimated according to

$$\varepsilon = \nu \Big\langle \frac{\partial u_i}{\partial x_j} + \frac{\partial u_j}{\partial x_i} \Big\rangle^2 \approx \frac{U_{\mathrm{w}} u_\tau^2}{h} \approx 0.5\,\mathrm{m}^2\,\mathrm{s}^{-3}, \tag{2.7}$$

where $u_\tau = (\tau_\mathrm{w}/\rho)^{1/2}$ is the friction velocity, and $\tau_\mathrm{w} = \mu\frac{\partial U}{\partial y}$ is the wall shear stress. The viscous lengthscale is defined as follows

$$\delta_\nu = \nu/u_\tau \approx 60\,\mu\mathrm{m}. \tag{2.8}$$

Here, for simplicity, we dropped the subscripts, and all quantities ρ, μ, ν and ε are based on properties of the liquid phase.

2.3.2. *Interface lengthscale*

In addition to turbulent lengthscales, we need to resolve an interfacial lengthscale (bubble radius) in two-phase simulations. There are two major mechanisms of bubble formation: turbulent fragmentation (Kolmogorov 1949; Hinze 1955) and instability of the air film due to liquid-liquid impact (Esmailizadeh & Mesler 1986; Pumphrey & Elmore 1990). In our simulations we resolve only the bubbles due to the first mechanism. This lengthscale can be estimated using the Kolmogorov-Hinze theory. We apply this theory to estimate the breakage of bubbles in a turbulent liquid flow. If the bubble diameter is larger than the Kolmogorov lengthscale, then the critical bubble radius (referred to as the Hinze scale) is given by

$$r_\mathrm{cr} = 2^{-8/5}\left(\frac{\sigma \mathrm{We}_\mathrm{cr}}{\rho_\mathrm{liq}}\right)^{3/5}\varepsilon^{-2/5} \quad \text{if} \quad 2r_\mathrm{cr} > \eta. \tag{2.9}$$

If the bubble diameter is smaller than the Kolmogorov lengthscale, then the critical bubble radius is given by

$$r_\mathrm{cr} \approx \left(\frac{\sigma \mathrm{We}_\mathrm{cr}}{\rho_\mathrm{liq}}\right)^{1/3}\varepsilon^{-1/3} \quad \text{if} \quad 2r_\mathrm{cr} < \eta. \tag{2.10}$$

In our case, the Hinze scale is much larger than the Kolmogorov lengthscale and the critical bubble radius is given by Eq. (2.9). For critical Weber number 4.7 (according to Deane & Stokes 2002), the critical bubble radius is $r_\mathrm{cr} \approx 3\,\mathrm{mm} \gg \eta$. Therefore, we choose conventional DNS resolution as in single-phase flows. We use a Cartesian grid with uniform mesh spacing in x and z directions, and stretched mesh in the y direction according to

$$y_j = \frac{h\tanh\left(\gamma(-1+\frac{2(j-1)}{N_y-1})\right)}{\tanh(\gamma)}, \tag{2.11}$$

where the stretching parameter γ is 2.9. Based on the viscous lengthscale in the liquid phase the grid resolution is $\Delta x^+ \approx 13$, $\Delta y^+_\mathrm{min} \approx 0.2$, $\Delta y^+_\mathrm{max} \approx 13$ and $\Delta z^+ \approx 7$. Such discretization results in at least 4 grid points per Hinze scale (8 points per bubble diameter) and 18 grid points per viscous sublayer.

Finally, the timestep is given from the stability constraint due to surface tension as it is more restrictive than the stability conditions due to convection and gravity terms (the viscous terms are treated implicitly):

$$\Delta t = \sqrt{\frac{\rho_\mathrm{liq}+\rho_\mathrm{gas}}{4\pi\sigma}}\Delta y_\mathrm{min}^{3/2} \approx 10^{-6}\,\mathrm{s}. \tag{2.12}$$

3. Results

To get a statistically developed flow we run the simulations for about 100 flow-through times. Figure 2(a) and Figure 2(b) show the time histories of the potential energy due

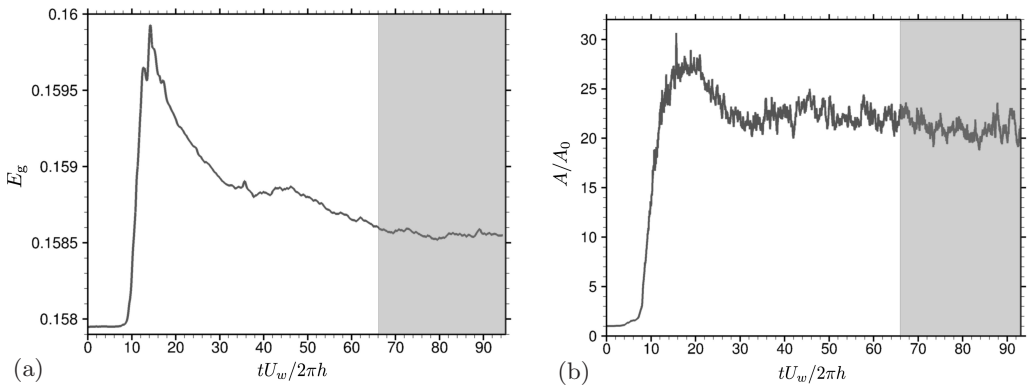

FIGURE 2. Time history of (a) potential energy due to gravity, $E_g = \int_V \rho(\mathbf{x},t)\mathbf{g}\cdot\mathbf{x}\,d\mathbf{x}$; (b) normalized area of the air-water interface A/A_0, where $A = \int_V \delta(\phi)|\nabla\phi|\,d\mathbf{x}$, ϕ is the level-set function. The gray box depicts a statistical sampling window.

to gravity and the total area of the air-water interface, respectively. Figure 2(a) shows that it takes about 70 flow-through times to achieve fully developed state, after which turbulent statistics are collected over 30 flow-through times (this region is depicted by the gray box). The maximum potential energy is about 1.3% of the initial value at the time of maximum deformation (around 15 flow-through times), and it is about 0.4% higher than its initial value at the fully developed state. Figure 2(b) shows the evolution of the gas-liquid interface area. Due to interface corrugation and generation of bubbles, the total area of the interface increases about 22 times compared to the initial area of the unperturbed interface.

Figure 3(a-d) show instantaneous snapshots of the interface (given by iso-surface $\psi = 0.5$). On the free surface, shear-induced oblique wave structures are observed (Figure 3(a)), then the interfacial waves grow in amplitude (Figure 3(b)), leading to breakup of the interface (Figure 3(c)). The air cavities are found underneath the free surface, trapped between the breaking interfacial waves. These air cavities are subsequently fragmented into air bubbles in the water. Finally, Figure 3(d) shows the interface at the fully developed state.

Figure 4 shows time- and streamwise-averaged flow for two cases: (a) a two-phase Couette flow and (b) a single-phase Couette water flow at the same Reynolds number of 8000. The color contours correspond to the streamwise component of the mean velocity, $\bar{u}$, while the wall-normal and spanwise components, $(\bar{v},\bar{w})$, are shown as vector plot. The maximum root-mean-square (rms) value of in-plane velocities represents (after 100 flow-through times) approximately 6-7% of the maximum streamwise velocity for both cases and does not diminish with time. For the single-phase Couette flow, secondary flow is represented by four large eddies, while for the two-phase case the secondary flow is more complex due to the effects of the interface. In our simulations the length of the computational domain, $2\pi h$, was chosen as in classical simulations of pressure-driven channel flow. However, it is known from studies of single-phase Couette flow (Lee & Kim 1991; Komminaho *et al.* 1996; Papavassiliou & Hanratty 1997) that the domain length should be much longer. In this work we focus on a study of interface/boundary layer interaction and leave the study of Couette flow in longer channels for future research.

Mean streamwise velocity profiles measured at $z/h = 1.5$, $z/h = 2.5$, $z/h = 3.5$ and $z/h = 4$ locations are shown in Figure 5. In addition to two-phase Couette results,

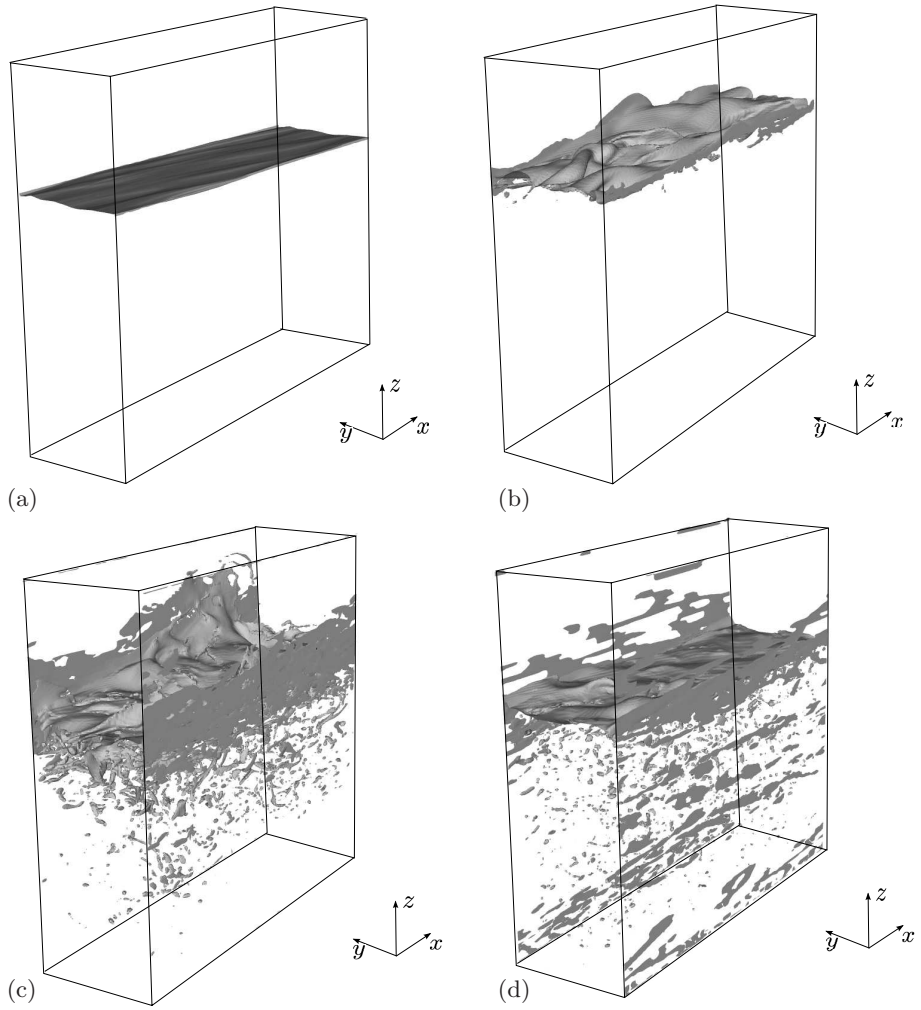

FIGURE 3. Snapshots of the air-water interface at different times: (a) $t^* = 5$; (b) $t^* = 10$; (c) $t^* = 15$; (d) $t^* = 60$.

we show the result of simulation for single-phase Couette flow at the same Reynolds number of 8000. Figure 5(a) shows velocity profiles in non-dimensional units, U/U_w versus y/h. Figure 5(b) shows the same data in non-dimensional viscous units according to $U^+ = (U - U_\mathrm{w})/u_\tau$ and $y^+ = (h - y)/\delta_\nu$. As seen from Figure 5(b), there is no collapse of the results for two-phase Couette flow with the log-law even for a velocity profile quite far from the interface at $z/h = 1.5$. Even for single-phase Couette flow, a particular profile of streamwise velocity does not necessarily collapse with the log-law owing to the presence of persistent roller structures. Only after averaging of velocity in a vertical direction does the velocity profile for single-phase Couette flow matches with the log-law.

Figure 6 shows the rms value of the streamwise turbulent intensity. The 2D field of the turbulent fluctuations is presented on the left, while 1D profiles at different locations $z/h = 1.5$, $z/h = 2.5$, $z/h = 3.5$ and $z/h = 4$ are presented on the right. Compared

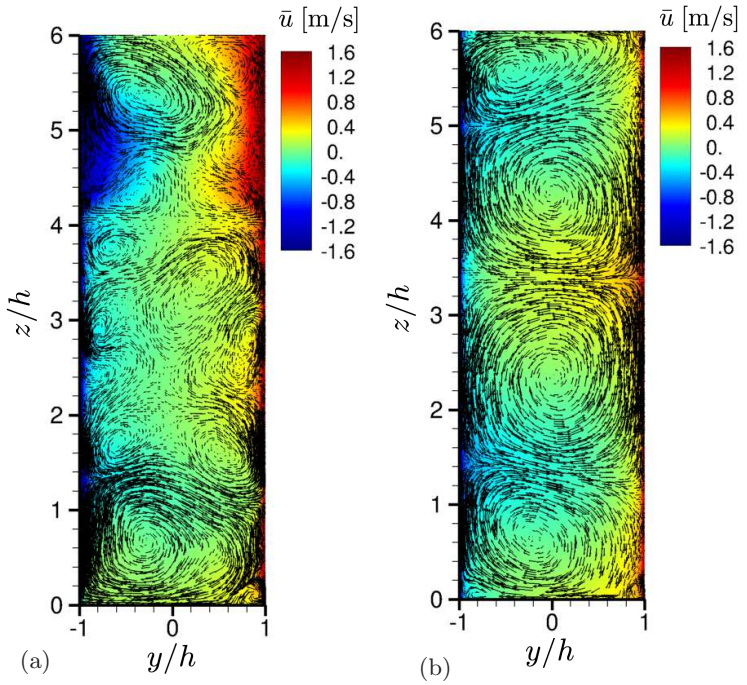

FIGURE 4. Turbulent statistics: time- and streamwise-averaged velocity field. Color plot shows the mean streamwise velocity; vector plot depicts mean in-plane flow. (a) Two-phase Couette flow at Re = 8000, We = 730 and Fr = 3.6; (b) Single-phase Couette flow at Re = 8000.

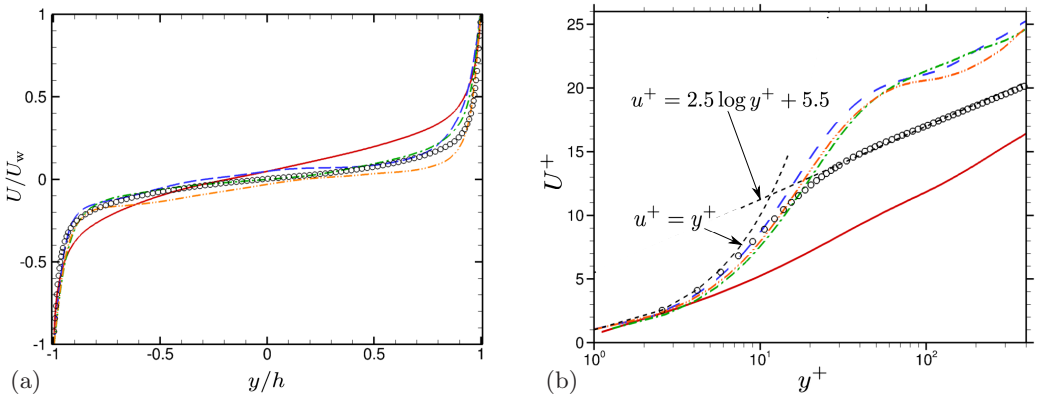

FIGURE 5. Turbulent statistics for two-phase Couette flow at Re = 8000, Fr = 3.6, We = 730: (a) mean streamwise velocity; (b) mean streamwise velocity in viscous units. Lines represent profiles at different depths: ———, $z/h = 4$; – – –, $z/h = 3.5$; – · –, $z/h = 2.5$; – · · –, $z/h = 1.5$. Symbols ∘ correspond to DNS results (also averaged in the vertical direction) for single-phase Couette water flow at the same Reynolds number.

to single-phase Couette flow at $z/h = 4$, amplification of turbulent intensity was found near the interface, whereas a diminished turbulent intensity was observed in the core region. Figure 7 and Figure 8 show rms values of the wall-normal and spanwise turbulent intensities, respectively. Note that for wall-normal and spanwise turbulent intensities, turbulence near the wall and near the interface (profile at $z/h = 4$) increases compared

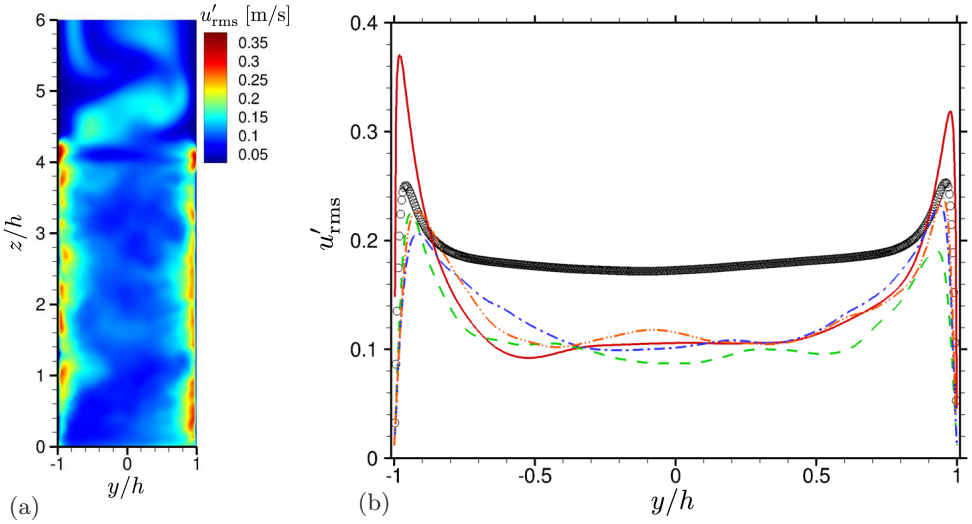

FIGURE 6. Turbulent statistics: rms of the streamwise velocity fluctuation. (a) 2D field; (b) 1D profiles at different depths: ———, $z/h = 4$; – – –, $z/h = 3.5$; – · –, $z/h = 2.5$; – · · –, $z/h = 1.5$. Symbols ∘ correspond to DNS results for single-phase Couette water flow.

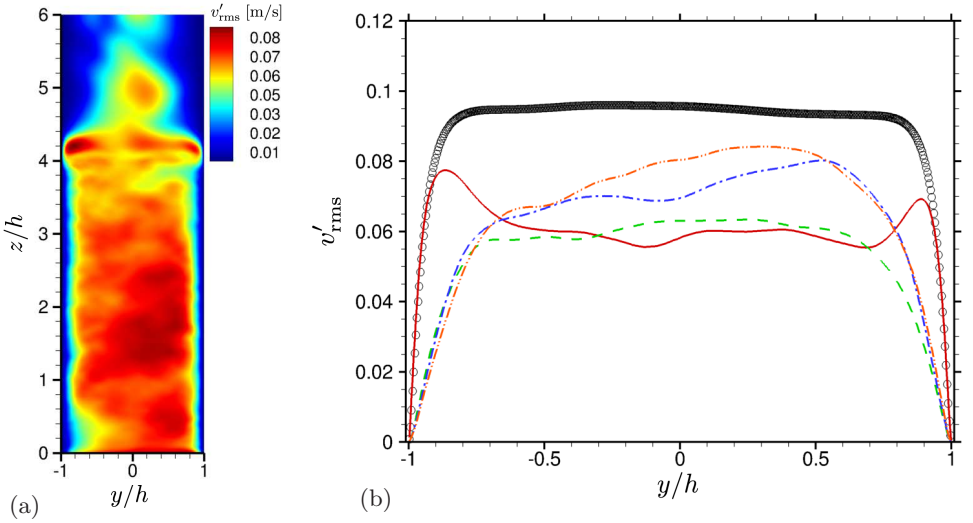

FIGURE 7. Turbulent statistics: rms of the wall-normal velocity fluctuation. (a) 2D field; (b) 1D profiles at different depths: ———, $z/h = 4$; – – –, $z/h = 3.5$; – · –, $z/h = 2.5$; – · · –, $z/h = 1.5$. Symbols ∘ correspond to DNS results for single-phase Couette water flow.

to turbulent intensity at other depths. However, the absolute value of turbulent intensity is larger for single-phase Couette flow.

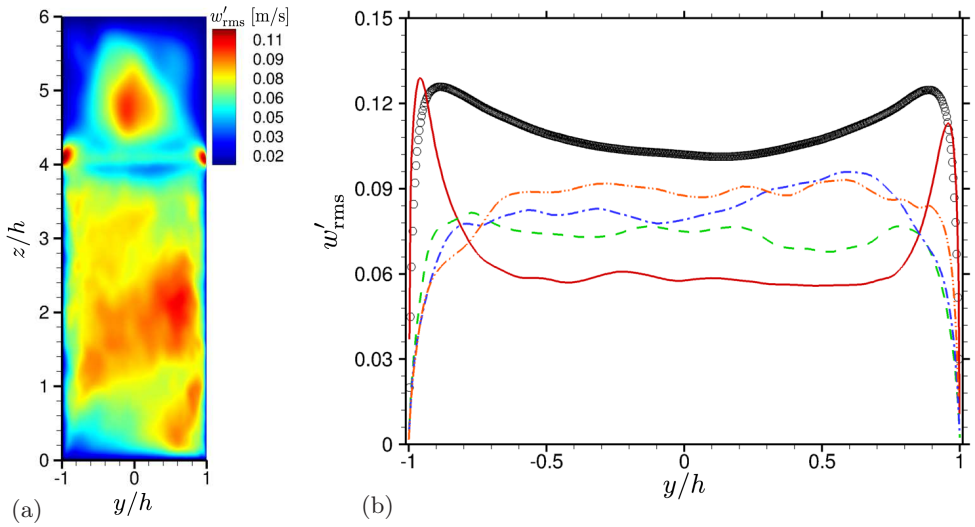

FIGURE 8. Turbulent statistics: rms of the vertical velocity fluctuation. (a) 2D field; (b) 1D profiles at different depths: ———, $z/h = 4$; – – –, $z/h = 3.5$; – · –, $z/h = 2.5$; – · · –, $z/h = 1.5$. Symbols ○ correspond to DNS results for single-phase Couette water flow.

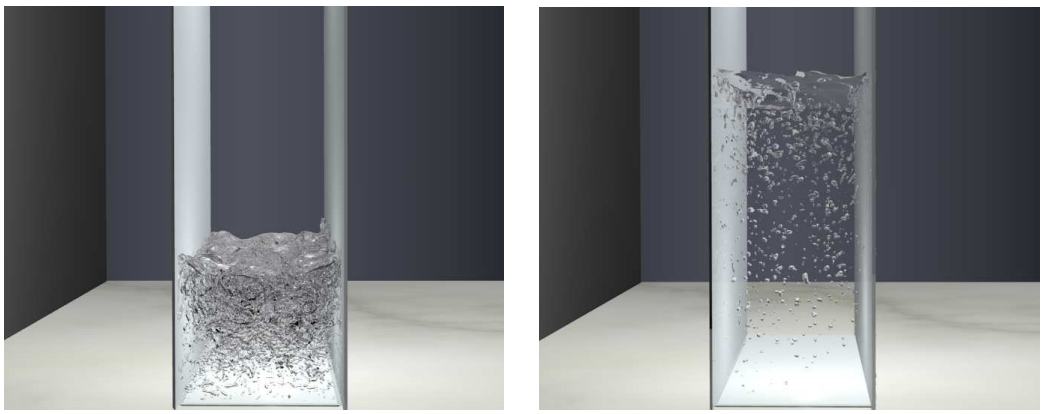

(a) (b)

FIGURE 9. Air-water interface at fully developed state: (a) Results for an aspect ratio of 1.57 and Re = 12000, We = 206, Fr = 3.8 (Kim *et al.* 2013); (b) Present results for an aspect ratio of 4 and Re = 8000, We = 730, Fr = 3.6.

4. Influence of the water depth

Figure 9 shows a comparison of the fully developed air-water interface from our previous results (Kim *et al.* 2013) (Figure 9(a)) and the current simulation (Figure 9(b)). The results on the left figure were obtained for an aspect ratio of 1.57, whereas in the current simulation the aspect ratio is 4. As seen, the simulation for the higher value of the aspect ratio predicts much less air entrainment. To confirm our hypothesis of the influence of the water depth on bubble density, we are currently running simulations for low and high values of the aspect ratio (1.57 and 8) for the same non-dimensional parameters: Reynolds, Weber and Froude numbers, as in the simulation presented in this work.

5. Conclusions

In this work we performed a numerical simulation of a two-phase Couette flow at a Reynolds number of 8000, Froude number of 3.6, Weber number of 730 and at realistic air-to-water density and viscosity ratios. Except for Reynolds number and water depth, the parameters of simulation correspond to experiments currently being performed at the University of Maryland. The VOF method has been used to predict interface dynamics. To achieve statistically state, two-phase simulations of Couette flow require much longer time compared to simulations of single-phase Couette flow. Amplification of turbulent intensity was found near the interface, whereas diminished turbulent intensity was observed in the core region. It was found that the bubble density depends on the water depth. To validate this result, in our ongoing work we compare numerical results obtained for different aspect ratios with experimental data. In addition, a simulation is being carried out with deeper water at an aspect ratio H_{liq}/h of 8 and the same non-dimensional parameters, Re = 8000, We = 730, Fr = 3.6.

Acknowledgments

The authors would like to express their gratitude to Dr. Ivan Bermejo-Moreno for his useful comments. The financial support of the Office of Naval Research is gratefully acknowledged. The authors also acknowledge computing time on the Mira cluster at Argonne Leadership Computing Facility (ALCF) and on the Certainty cluster at Stanford (MRI-R2 NSF Award 0960306).

REFERENCES

Brackbill, J., Kothe, D. & Zemach, C. 1992 A continuum method for modeling surface tension. *J. Comput. Phys.* **100**, 335–354.

Charru, F. & Hinch, J. E. 2000 Phase diagrama of interfacial instabilities in a two-layer Couette flow and mechanism of the long-wave instability. *J. Fluid Mech.* **414**, 195–223.

Coward, A. V., Renardy, Y. Y., Renardy, M. & Richards, J. R. 1997 Temporal evolution of periodic disturbances in two-layer Couette flow. *J. Comput. Phys.* **132**, 346–361.

Deane, G. B. & Stokes, M. D. 2002 Scale dependence of bubble creation mechanisms in breaking waves. *Nature* **418**, 839–844.

Esmailizadeh, L. & Mesler, R. 1986 Bubble entrainment with drops. *J. Colloid Interface Sci.* **110**, 561–574.

Francois, M. M., Cummins, S. J., Dendy, E. D., Kothe, D. B., Sicilian, J. M. & Williams, M. W. 2006 A balanced-force algorithm for continuous and sharp interfacial surface tension models within a volume tracking framework. *J. Comput. Phys.* **213**, 141–173.

Fulgosi, M., Lakehal, D., Banerjee, S. & De Angelis, V. 2003 Direct numerical simulation of turbulence in a sheared air-water flow with a deformable interface. *J. Fluid Mech.* **482**, 319–345.

Hinze, J. 1955 Fundamentals of the hydrodynamic mechanism of splitting in dispersion processes. *AIChE J.* **1**, 289–295.

Iwasaki, T., Nishimura, K., Tanaka, M. & Hagiwara, Y. 2001 Direct

numerical simulation of turbulent Couette flow with immiscible droplets. *Int. J. Heat Fluid Flow* **22**, 332–342.

Kim, D., Mani, A. & Moin, P. 2012 Numerical simulation of wave breaking in turbulent two-phase Couette flow. *Annual Research Briefs*, Center for Turbulence Research, Stanford University, pp. 171–178.

Kim, D., Mani, A. & Moin, P. 2013 Numerical simulation of bubble formation by breaking waves in turbulent two-phase Couette flow. *Annual Research Briefs*, Center for Turbulence Research, Stanford University, pp. 37–46.

Kolmogorov, A. 1949 On the breakage of drops in a turbulent flow. *Dokl. Akad. Nauk. SSSR* **66**, 825–828.

Komminaho, J., Lundbladh, A. & Johansson, A. V. 1996 Very large structures in plane turbulent Couette flow. *J. Fluid Mech.* **320**, 259–285.

Lee, M. & Kim, J. 1991 The structure of turbulence in a simulated plane Couette flow. In *Eighth Symp. on Turbulent Shear Flows*, pp. 531–536.

Li, J., Renardy, Y. Y. & Renardy, M. 2000 Numerical simulation of breakup of a viscous drop in simple shear flow through a volume-of-fluid method. *Phys. Fluids* **12**, 269–282.

Liu, S., Kermani, A., Shen, L. & Yue, D. K. P. 2009 Investigation of coupled air-water turbulent boundary layers using direct numerical simulations. *Phys. Fluids* **21**, 62–108.

Masnadi, N., Washuta, N., Wang, A. & Duncan, J. 2013 The interaction of a turbulent ship-hull boundary layer and a free surface. *Bull. Am. Phys. Soc.* **58**.

Papavassiliou, D. V. & Hanratty, T. J. 1997 Interpretation of large-scale structures observed in a turbulent plane Couette flow. *Int. J. Heat Fluid Flow* **18**, 55–69.

Pumphrey, H. C. & Elmore, P. A. 1990 The entrainment of bubbles by drop impacts. *J. Fluid Mech.* **220**, 539–567.

Rallison, J. 1984 The deformation of small viscous drops and bubbles in shear flows. *Ann. Rev. Fluid Mech.* **16**, 45–66.

Renardy, Y., Cristini, V. & Li, J. 2002 Drop fragment distributions under shear with inertia. *Int. J. Multiphase Flow* **28**, 1125–1147.

Sethian, J. 1999 Fast marching methods. *SIAM Review* **41**, 199–235.

Washuta, N., Masnadi, N. & Duncan, J. 2014 The turbulent boundary layer on a horizontally moving, partially submerged, surface-piercing vertical wall. In *Symposium on Naval Hydrodynamics,*, pp. 195–213.